Applied Catalysis B: Environmental 186 (2016) 77–87

Contents lists available at ScienceDirect

Applied Catalysis B: Environmental

journal homepage: www.elsevier.com/locate/apcatb

Enhanced disinfection application of Ag-modified g-C_3N_4 composite under visible light

Shuanglong Ma, Sihui Zhan*, Yanan Jia, Qiang Shi, Qixing Zhou*

Key Laboratory of Pollution Processes and Environmental Criteria (Ministry of Education), College of Environmental Science and Engineering, Nankai University, Tianjin 300071, PR China

ARTICLE INFO

Article history:
Received 6 September 2015
Received in revised form
20 December 2015
Accepted 30 December 2015
Available online 4 January 2016

Keywords:
Photocatalytic
Visible light
Disinfection
g-C_3N_4
Ag nanoparticles

ABSTRACT

Ag/g-C_3N_4 composite photocatalyst, which was synthesized by thermal polymerization of melamine precursor combined with the photo-assisted reduction method, was applied as an efficient visible-light-driven photocatalyst for inactivating *Escherichia coli* (*E. coli*). The composite photocatalysts exhibited significantly enhanced photocatalytic disinfection efficiency than pure g-C_3N_4 powders. The mechanism of enhanced disinfection activity was systematically investigated by UV–visible diffuse reflectance spectra, photoluminescence spectra, and photo-electrochemical methods including photogenerated current densities, electrochemical impedance spectroscopy (EIS) spectra and Mott–Schottky plots. The enhanced photocatalytic bactericidal effect was attributed to the hybrid effect from Ag and g-C_3N_4, which resulted in enhanced adsorption of visible light, reduced recombination of free charges, rapid separation and transportation of photogenerated electrons–holes. The disinfection mechanism was studied by employing chemical scavengers and ESR technology, indicating the important role of h^+ and e^-. Considering the bulk availability and excellent disinfection activity of Ag/g-C_3N_4, it is a promising solar-driven photocatalyst for cleaning microbial contaminated water in practice.

1. Introduction

Microbial contamination is always harmful to human health since the existence of human society. Many kinds of bacteria can result in serious illness and even death for humans [1]. Therefore, it is significant and necessary to develop effective, low cost and environmentally benign biocides [2–4]. Since the photon-based disinfection method by platinum-doped TiO_2 mediated photocatalysis was first reported in 1985, photocatalytic disinfection has been extensively investigated and considered as one of the most promising disinfection processes [5,6]. By employing photocatalyst, photo-disinfection technique has been emerged as a preferable candidate compared with traditional bacterial inactivation methods such as chlorination and UV irradiation. However, chlorination is not environmentally benign and sustainable due to the production of carcinogenic disinfection byproducts and the existence of some free chlorine-resistant bacteria such as *Mycobacterium avium* [7]. In addition, UV light is not effective for some UV-resistant bacteria and the hazards of direct and intensive use of UV radiation restrict its application [8–10].

Currently, it is still a significant challenge to develop efficient, cost-effective, environmentally benign visible-light-responsive photocatalysts [11]. To reach the desired efficiency, the ideal photocatalyst should possess a high photo- and chemical stability, a wide light adsorption range covering the entire spectrum of sunlight, minimal recombination of photogenerated charge carriers, and facile preparation method [12]. Recently, graphitic carbon nitride (g-C_3N_4), a novel metal-free polymeric photocatalyst with narrow band gap energy of 2.7 eV, was reported by Wang et al., exhibiting a good performance for hydrogen and oxygen production by water splitting under visible light [13]. Graphitic C_3N_4 has attracted extensive attentions in water splitting [14] and environment purification [15] due to its high stability, bulk availability, low cost, and outstanding optical property. However, the photocatalytic efficiency of pure g-C_3N_4 is limited due to its fast recombination of photogenerated electron–hole pairs, low visible-light utilization efficiency, and small surface area [16]. Among the novel photocatalysts under investigation, one can use two different semiconductors [17], semiconductor-metal [18], or semiconductor-nonmetal [19] composite to overcome the above mentioned disadvantages. Therefore, many methods have been investigated to improve the visible light photocatalytic efficiency of g-C_3N_4 such as combining with semiconductors [20–23], doping with non-metals [24–26], and coupling with metals [27–29].

* Corresponding authors. Fax: +86 22 66229562.
E-mail addresses: sihuizhan@nankai.edu.cn (S. Zhan), zhouqx@nankai.edu.cn (Q. Zhou).

http://dx.doi.org/10.1016/j.apcatb.2015.12.051
0926-3373/

By modifying a semiconductor with noble metal nanoparticles including silver, gold, and platinum, the photocatalytic activity of the semiconductor can be significantly improved. Therefore, plasmonic nanostructures which combine the advantages of semiconductor photocatalysts and noble metal species have recently attracted a great deal of interest [30]. Among them, the nanostructures of Ag species embedded in a matrix of g-C_3N_4, can increase the photocatalytic activity of g-C_3N_4 [18,31,32]. It is generally accepted that the surface plasmon resonance (SPR) effect contributes to the observed enhancement of photocatalytic activity after noble metal modification [33]. It had been proposed that the SPR effect could induce the formation of an intensive electromagnetic, which interacted with the semiconductor and further enhanced the formation rates of h^+ and e^- in the semiconductor. In addition, the noble metal particles could act as electron sinks, trapping free electron and thereby reducing the recombination rates of photogenerated electrons–holes. It was also reported that the plasmonic nanostructures could scatter resonant photons efficiently, leading to longer optical path lengths for photons in the photocatalyst, which caused enhanced evolution rates of photoinduced charge carriers [34].

Although the photocatalytic bacterial inactivation effect of g-C_3N_4 have been discussed in the early reports [15,25], the inactivation efficiency still needed to be further improved owing to the low visible-light adsorption and rapid recombination of charge carriers. Herein, for achieving a better inactivation result and utilizing the abundant solar energy, Ag/g-C_3N_4 heterostructures were synthesized by the method combining thermal polymerization of melamine precursor with photo-reduction approach. The plasmonic composites are expected to possess better disinfection effect than pure g-C_3N_4 for the SPR effect from Ag nanoparticles and hybrid effect from g-C_3N_4. On the one hand, the intense local electromagnetic fields caused by the SPR effects of Ag nanoparticles can accelerate the formation rate of charge carriers with g-C_3N_4 [34], and the Fermi level of silver promotes the separation of holes and electrons [35], further increasing the quantum efficiency of g-C_3N_4. On the other hand, it is widely accepted that silver itself is a superior antibacterial agent [36]. The photocatalysts are characterized by TEM, XRD, FTIR, XPS, and BET analyses. The bactericidal effects toward *Escherichia coli* were investigated using standard plate count, laser scanning fluorescence microscopy, and SEM methods. It can be found that Ag/g-C_3N_4 composites exhibited significantly better photocatalytic disinfection effect than pure g-C_3N_4. The promotion mechanisms were also systematically investigated by photo-electrochemical methods including photogenerated current densities, electrochemical impedance spectroscopy (EIS) spectra and Mott–Schottky plots. The generation of reactive species were measured using chemical scavengers and ESR technique, indicating the important roles of h^+, e^- and $^{\bullet}O_2^-$ during photocatalytic disinfection process.

2. Experimental

2.1. Materials

All chemicals used in this work are analytical grade. All chemicals were used as-received without any further purification. Silver nitrate ($AgNO_3$), melamine ($C_3H_6N_6$), and anhydrous ethanol (C_2H_5OH) were purchased from Jiangtian Chemical Technology Co., Ltd. (Tianjin, China).

2.2. Synthesis of Ag/g-C_3N_4 photocatalysts

Bulk g-C_3N_4 powder was synthesized according to the early report by Wang et al. [37]. Typically, 10 g melamine was put into a crucible with a lid under ambient pressure in air, and then the crucible was heated at 550 °C for 4 h with a heating rate of 2.3 °C/min in a muffle furnace. After cooling naturally, the yellow products were milled into powder in an agate mortar for further experiments. The g-C_3N_4 nanosheets were prepared by a mixed-solvent exfoliation method [38]. Particularly, 1.5 g bulk g-C_3N_4 powders were added into 450 mL solvents which were composed of ethanol and deionized water with a volume ration of 3:1. After sonicated for 10 h, the yellow suspension was centrifuged at 3000 rpm for 10 min to remove the residual g-C_3N_4 nanoparticles. Ultimately, the exfoliated g-C_3N_4 nanosheets were collected by centrifuging at 10000 rpm for 5 min and dried at 80 °C for 24 h.

The preparation of Ag/g-C_3N_4 plasmonic photocatalysts is described as follows: 0.5 g of as-prepared g-C_3N_4 was ultrasonically dispersed in 15 mL of deionized water for 30 min. Then, 5 mL of $AgNO_3$ aqueous solution with different concentrations (0.79, 1.57, 3.15, 4.72, 6.30, 7.87 mg/mL) was dropwise added to the g-C_3N_4 solution, leading to different weight percentages of Ag in the initial photocatalyst precursors (0.5, 1, 2, 3, 4, and 5 wt%). Then, the resultant suspension was stirred for 2 h under the irradiation of a 300 W Xenon arc lamp (CEL-HXF300, Ceaulight, Beijing). The final suspension was centrifuged and washed with deionized water three times for purification, and then the product was dried in an oven at 80 °C for 24 h. The Ag/g-C_3N_4 composites were marked as Ag(*X*)/g-C_3N_4. *X* indicates Ag/g-C_3N_4 mass ratio in preparation, which were 0.5, 1, 2, 3, 4, and 5, respectively.

2.3. Characterizations

The X-ray diffraction (XRD) patterns of samples were recorded via an X-ray diffractometer (Rigaku D/Max 2500PC) with a CuKα radiation. FTIR spectra were recorded on a Nicolet 5DX-FTIR spectrometer using KBr method. The morphology and elemental analysis of samples were observed through transmission electron microscopy (TEM, JEOL Model JEM-1200EX). The morphology of bacteria was imaged by scanning electron microscopy (Hitachi S-4800, Japan). X-ray photo-electron spectroscopy (XPS) spectra were collected on an ESCALAB250 multi-technique X-ray photoelectron spectrometer using a monochromatic Al Kα X-ray source. The Ag ions concentration was measured using ICP-MS (X7 Series, Thermo Electron Corporation, USA). Light absorption (reflectance) spectra were recorded by UV–vis–NIR diffuse reflectance spectrum (Shimadzu Corporation, UV-3600, Japan). The room-temperature photoluminescence (PL) spectra of g-C_3N_4 and Ag/g-C_3N_4 photocatalysts were investigated using an Edinburgh Instruments FLS920P equipped with a Xe lamp-920 with an excitation wavelength of 368 nm. Electrochemical and photoelectrochemical performances were measured in a three electrode quartz cells system including a platinum plate as counter electrode and saturated calomel electrode (SCE) as reference electrode, and ITO glass deposited with g-C_3N_4 and Ag/g-C_3N_4 as the working electrode, respectively. The electrolyte was 0.1 M Na_2SO_4. The photoelectrochemical experiment results were recorded using an electrochemical station (CHI660B, Shanghai Chenhua, China). The visible light irradiation was obtained from a 300 W Xenon arc lamp (CEL-HXF300, Ceaulight, Beijing). ESR signals of spin-trapped paramagnetic species with 5,5-diemthyl-1-pyrroline N-oxide (DMPO) were recorded with a Magnet Tech MS400 spectrometer. The photocurrent responses of the photocatalysts as visible light on and off were measured at 0.0 V. Electrochemical impedance spectra (EIS) were measured at 0.0 V over the frequency range of 0.05–10^5 Hz with an AC voltage of 5 mV. Mott–Schottky plots were measured at the potential range of −1.0 V to 1.0 V and the frequency of 1000 Hz with an AC voltage of 10 mV.

2.4. Disinfection activity

Gram-negative *E. coli* was used as model bacteria. The bacteria were grown in nutrient broth at 37 °C for 15 h to yield a cell count of approximately 10^9 colony forming units (cfu)/mL. Then bacterial cells were collected by centrifugation (5000 × *g* for 10 min) and resuspended in sterile 0.85% (wt/vol) saline solution. The bacteria concentration for bactericidal study was 10^7 cfu/mL, which was adjusted by gradient dilution using 0.85% (wt/vol) saline solution.

Typically, 250 μL of photocatalyst saline solution (4 mg/mL) was added to a 50 mL beaker containing 10 mL of bacteria solution (10^7 cfu/mL). The bacteria and photocatalyst were mixed on a magnetic stirrer at room temperature, and simultaneously irradiated by a 300 W Xenon arc lamp (CEL-HXF300, Ceaulight, Beijing) with a UV cutoff (λ < 420 nm). The spectra of the xenon arc lamps without and with a UV cutoff (λ < 420 nm) are shown in Fig. S1. As the reaction proceeded, the mixture was carefully pipetted out at a scheduled interval and the bacteria concentrations were determined by the standard plate count method. The plates were incubated at 37 °C for 24 h. The number of colonies was enumerated through visual inspection. There were a series of experiments conducted in the dark at the same situations as the dark controls. The light control group was carried out in the absence of photocatalyst. All the experiments were repeated for three times.

2.5. Fluorescent-based cell live/dead test

The bacteria death analysis was also ascertained by fluorescent-based cell live/dead test. The mixture of log phase cells (10^9 cfu/mL) and photocatalyst (100 μg/mL) were mixed on a magnetic stirrer at room temperature, and simultaneously irradiated by a 300 W Xenon arc lamp with a UV cutoff (λ < 420 nm) for 1.5 h. Then the mixture were stained with PI (propidium iodide) and SYTO9 (LIVE/DEAD Baclight Bacterial Viability kit) according to the instruction of the kit, and imaged using a laser scanning fluorescence microscopy (Olympus, FV1000). The cell suspension without photocatalysts in presence of light was taken as control.

2.6. SEM observation of bacteria

SEM was used to visualize the interaction between photocatalyst and bacteria. The photo-treated bacteria at different irradiation time (0, 30, 45, 60, 75, and 90 min) were fixed on silicon pellet with 2.5% glutaraldehyde solution in 4 °C overnight. Then the samples were sequentially dehydrated with 30, 50, 70, 90, and 100% ethanol for 20 min, respectively. The samples were lyophilized, gold sputter-coated, and visualized using a SEM.

3. Results and discussion

3.1. Characterizations of photocatalysts

The detailed morphology and microstructure of pure and hybrid photocatalysts were imaged using TEM. The typical TEM images of g-C_3N_4, Ag(1)/g-C_3N_4, Ag(3)/g-C_3N_4, and Ag(5)/g-C_3N_4, are shown in Fig. 1. Fig. 1a exhibits the platelet-like morphology of g-C_3N_4, which was very similar to that of graphene. The morphology of Ag(1)/g-C_3N_4 is shown in Fig. 1b, which also displayed a sheet-like structure. However, Ag nanoparticles are not observed on the surface of g-C_3N_4. It was possibly attributed to that low Ag modifying amount resulted into very small Ag nanoparticles, which were difficult to be observed. As shown in Fig. 1c and d, for Ag(3)/g-C_3N_4 and Ag(5)/g-C_3N_4, Ag nanoparticles were well dispersed on the g-C_3N_4 nanosheets. With the increase of Ag modifying amount, more Ag nanoparticles were deposited on the surface of g-C_3N_4 for Ag(5)/g-C_3N_4 compared with Ag(3)/g-C_3N_4. Fig. 2a is a representative TEM image of Ag(3)/g-C_3N_4, with a corresponding energy-dispersive X-ray spectroscopy (EDS) elemental mapping for C (Fig. 2b), N (Fig. 2c), and Ag (Fig. 2d). A brighter area in the elemental map indicated a higher concentration of the corresponding element in that area. Different elements were shown in different colors in order to identify their positions within the photocatalysts. Obviously, the C and N distributions were uniform and continuous, resembling the morphology of g-C_3N_4 nanosheets. In contrast, the distribution of Ag nanoparticles was discrete, indicating a hierarchical heterostructure of nano-Ag well-dispersed on the surface of g-C_3N_4 nanosheets. All of these results confirmed the successful synthesis of Ag/g-C_3N_4 composite photocatalysts.

In the XRD patterns (Fig. S2), for all the prepared samples, pentagram represented two characteristic peaks of g-C_3N_4. The peaks at 13.0° and 27.6° can be indexed to the (1 0 0) and (0 0 2) diffraction plane, corresponding to the in-plane structural packing motif with a period of 0.675 nm and interlayer-stacking with an interlayer distance of d = 0.33 nm, respectively [16]. For all the Ag/g-C_3N_4 composites, the characteristic peaks of crystal Ag were not directly observed in the patterns. This phenomenon was possibly attributed to the low Ag modifying amounts and its characteristic peaks were too low to recognize in the background, which was in accordance with the early report by Bu et al. [18]. The FTIR spectra of g-C_3N_4 and Ag(3)/g-C_3N_4 are shown in Fig. S3. For g-C_3N_4, several absorption bands at 1700–1000 cm^{-1} were attributed to either C═N or C—N stretching vibrations in the CN heterocycles. The broad adsorption band centered at 3200 cm^{-1} originated from the N—H stretching vibration mode. The sharp peak at 813 cm^{-1} was associated with the bending vibration mode of *s*-triazine, suggesting that the local structure of the as-prepared g-C_3N_4 was composed of heptazine. After photodeposition of silver nanoparticles, all the characteristic vibration peaks of g-C_3N_4 can still be found in the Ag(3)/g-C_3N_4 composite, indicating that the chemical structure of g-C_3N_4 remains unchanged after Ag modification [16].

To investigate the surface composition and chemical state of different element, g-C_3N_4 and Ag(3)/g-C_3N_4 were analyzed by XPS. Fig. S4 displays the survey, C 1s, N 1s, and Ag 3d spectra. The survey spectra of g-C_3N_4 and Ag(3)/g-C_3N_4 suggested that C, N, and O existed on the surface of g-C_3N_4, and C, N, O and Ag on the surface of Ag(3)/g-C_3N_4. As shown in Fig. S4b, for both samples, the C 1s XPS spectra had two distinct peaks at 288.3 and 284.6 eV. The first at 284.6 eV was related to the C—C bonding of reference carbon on the surface [14]. The second at 288.3 eV was ascribed to carbon atoms bonded with three adjacent nitrogen atoms in the g-C_3N_4 lattice [39]. According to Fig. S4c, the broad N 1s peak of both samples can be separated into three component peaks centered at 398.8, 400.3, 404.7 eV, respectively. The peak at 398.8 eV was due to the sp^2-hybridized aromatic triazine rings (C═N—C) [14]. The peak at 400.3 eV was attributed to the tertiary nitrogen (N-$(C)_3$) or amino functional groups carrying hydrogen ($(C)_2$-NH) [16]. The peak at 404.7 eV was ascribed to charging effects or positive charge localization in heterocycles [40]. As shown in Fig. S4d, the two peaks of an Ag 3 d level with binding energies 374.3 eV ($3d_{3/2}$) and 368.3 eV ($3d_{5/2}$) and spin energy separation of 6.0 eV corresponded to metallic silver Ag [16]. All the above analyses further verified the successful synthesis of sp^2-bonded graphitic carbon nitride nanosheet and the deposition of Ag nanoparticles on the surface of it.

3.2. Photocatalytic disinfection performance

The disinfection activities of as-prepared photocatalysts (g-C_3N_4, Ag(0.5)/g-C_3N_4, Ag(1)/g-C_3N_4, Ag(2)/g-C_3N_4, Ag(3)/g-C_3N_4, Ag(4)/g-C_3N_4 and Ag(5)/g-C_3N_4) were evaluated using *E. coli* as model organism. As shown in Fig. 3a, all the photocatalysts showed negligible disinfection efficiencies in the dark, despite that Ag(5)/g-

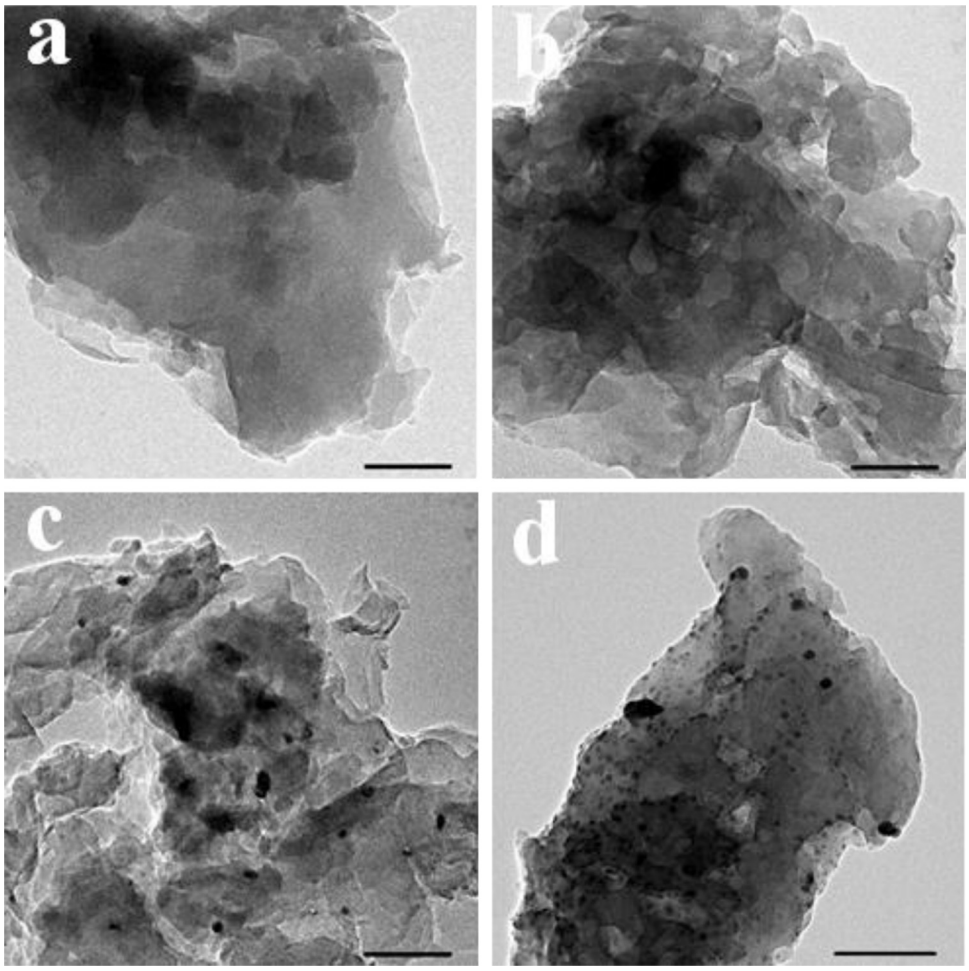

Fig. 1. TEM images of g-C_3N_4 (a), Ag(1)/g-C_3N_4 (b), Ag(3)/g-C_3N_4 (c), and Ag(5)/g-C_3N_4 (d). The scale bar is 100 nm.

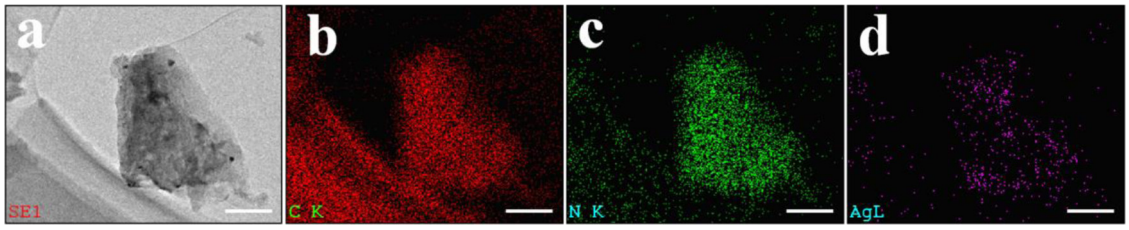

Fig. 2. TEM image of Ag(3)/g-C_3N_4 (a), and corresponding energy-dispersive X-ray spectroscopy (EDS) elemental mapping for C (b), N (c), and Ag (d). The scale bar is 100 nm.

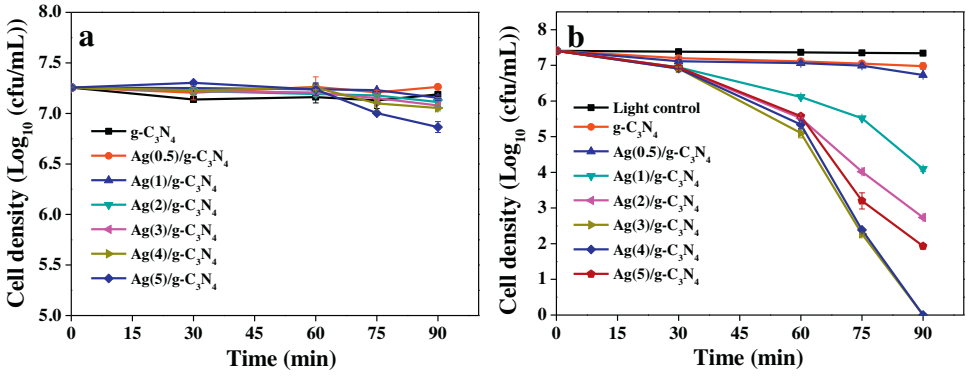

Fig. 3. (a) Inactivation efficiency toward *E. coli* (10^7 cfu/mL) with as-prepared samples (100 μg/mL) in the dark, (b) photocatalytic inactivation efficiency toward *E. coli* (10^7 cfu/mL) with the as-prepared samples (100 μg/mL) under visible light irradiation.

C_3N_4 displayed only about 0.4 log of inactivated *E. coli* cells. This result suggested that g-C_3N_4 itself had no cytotoxicity to *E. coli* in the dark. Additionally, although Ag nanoparticles were well accepted with antibacterial properties, Ag/g-C_3N_4 composites in this work exhibited almost negligible disinfection efficiencies, possibly attributing to the very low Ag doping amounts. Fig. 3b illustrates the disinfection results of *E. coli* exposed to as-prepared samples under visible light irradiation. It was found that almost no *E. coli* was inactivated in the light control (visible light irradiation without photocatalyst). The g-C_3N_4 displayed very low disinfection efficiency, and only about 0.4 log of *E. coli* cells were inactivated after 90 min of visible light irradiation. As for Ag/g-C_3N_4 composites, the bactericidal efficiency had been significantly enhanced compared with that of g-C_3N_4. The photocatalytic disinfection efficiency of Ag/g-C_3N_4 increased with Ag doping from 0.5 to 3 wt%, and further increasing Ag doping to 5%, the disinfection efficiency decreased. Concretely, over period of 75 min visible light irradiation, the quantity of viable bacteria is $10^{6.99}$, $10^{5.52}$, $10^{4.02}$, $10^{2.27}$, $10^{2.39}$ and $10^{3.20}$ for Ag(0.5)/g-C_3N_4, Ag(1)/g-C_3N_4, Ag(2)/g-C_3N_4, Ag(3)/g-C_3N_4, Ag(4)/g-C_3N_4 and Ag(5)/g-C_3N_4, respectively, indicating the best disinfection efficiency of Ag(3)/g-C_3N_4. This result suggested that the interaction between g-C_3N_4 and Ag nanoparticles played an important role in the enhancement of photocatalytic disinfection efficiency. As shown in Fig. 1, more Ag nanoparticles were deposited on the surface of g-C_3N_4 as the Ag loading amount increased from 3% to 5%. The possible interpretation for the above disinfection tendency was that excess Ag nanoparticles could act as recombination centers, or occupy the reactive sites of g-C_3N_4, resulting in the decreased efficiency of charge separation and bacteria adsorption capacity. Thus, the Ag amount was significant for enhancing the disinfection efficiency. One should make a balance between the much more trapping sites in turn favoring the recombination of electron–hole pairs and very fewer electron trapping centers leading to low separation rate of interfacial charges [31]. In this work, the optimal doping amount of Ag species on the surface of g-C_3N_4 was 3% according to the disinfection efficiency. Therefore, in the following parts, Ag(3)/g-C_3N_4 was selected to further study the influences of pH and humic acid on the disinfection efficiency, the changes of bacterial morphology, and the underlying mechanism for enhanced disinfection efficiency of composite photocatalysts.

In addition to the standard CFU counting method, fluorescent-based cell live/dead test was conducted by a laser scanning fluorescence microscopy to further verify the disinfection tendency of as-prepared photocatalysts. SYTO9 and PI, two fluorescent nucleic acid dyes, were employed to stain the DNA of *E. coli*. SYTO9 is a cell-permeable green-fluorescent stain which labels both live and dead bacteria, whereas PI is a cell-impermeable red-fluorescent stain that only labels cells with compromised cellular membranes. As shown in Fig. 4, there were few dead cells in the light control. For Ag(3)/g-C_3N_4 in the dark treatment group, only a small number of dead cells were observed. The above staining results were consistent with these of CFU counting method. As expected, for Ag(1)/g-C_3N_4, Ag(3)/g-C_3N_4, and Ag(5)/g-C_3N_4 treatment groups, the treated cells exhibited much more red fluorescence than these of light control and Ag(3)/g-C_3N_4 in the dark treatment. At the same experimental condition, in the presence of Ag(3)/g-C_3N_4, *E. coli* cells displayed the most red fluorescence than these of Ag(1)/g-C_3N_4 and Ag(5)/g-C_3N_4 treatments, indicating that Ag(3)/g-C_3N_4 possessed the best disinfection efficiency. In addition, Ag(5)/g-C_3N_4 showed better bactericidal activity than Ag(1)/g-C_3N_4, which also agreed with the result of CFU counting method. All the above results demonstrated that Ag/g-C_3N_4 composite photocatalysts had better disinfection efficiency than pure g-C_3N_4, among which the Ag(3)/g-C_3N_4 exhibited the best bactericidal result.

3.3. Ag ion leaking experiments

As well known, nano-Ag and Ag ions exhibit bactericidal activity toward many kinds of bacteria. Before conducting the Ag ion leaking experiment during the disinfection process, we first studied the bactericidal activity (under illumination) of a series of nano-Ag(*X*) and Ag^+(*X*) ($AgNO_3$) with different Ag and Ag ions concentrations which were equivalent to the designed Ag amounts in Ag(*X*)/g-C_3N_4 composite photocatalysts. In Fig. S5a, nano-Ag with different Ag concentrations exhibited almost negligible bactericidal effects, which were significantly lower than these of Ag/g-C_3N_4 with the same Ag doping amounts. As shown in Fig. S5b, Ag ions exhibited bactericidal effect toward *E. coli* in a dose-dependent manner. However, Ag(0.5) and Ag(1) almost had no bactericidal effect which was possibly attributed to their low Ag ions concentration. With the increase of Ag ions concentration, the Ag(2), Ag(3), Ag(4) and Ag(5) groups displayed 0.24, 0.56, 2.41, and 3.81 log of inactivated *E. coli* cells, respectively. However, the composite photocatalysts including Ag(2)/g-C_3N_4, Ag(3)/g-C_3N_4, Ag(4)/g-C_3N_4, and Ag(5)/g-C_3N_4 exhibited 4.67, 7.41, 7.41, and 5.48 log of inactivated *E. coli* cells under the same situation, respectively (Fig. 3b). Obviously, the composite photocatalysts exhibited far better bactericidal effect than the corresponding Ag ion.

For Ag(3)/g-C_3N_4, even if the designed amounts of Ag species in the composite photocatalyst were all released from it, the contribution of leaking Ag ions to the bactericidal effect was only 0.56 log, which was significantly lower than that of Ag(3)/g-C_3N_4 about 7.41 log. Furthermore, the Ag ion leaking from Ag/g-C_3N_4 in saline solution without *E. coli* cells and with *E. coli* cells (10^7 cfu/mL) was investigated as shown in Fig. S6. It can be observed that the Ag ions leaking were not proportional to the amounts of Ag doped. The Ag ions leaking in *E. coli* saline solution was higher than that in saline solution without *E. coli*. It appears that all the Ag ions leaking concentrations were very low with the highest one about 0.25 mg/L. According to the bactericidal effect of Ag ions in Fig. S5b, 0.5 mg/L Ag ions treatment almost had no bactericidal effect toward *E. coli*. Therefore, the amounts of Ag ion leaking from the composite photocatalysts here had little contribution to the bactericidal effect of Ag/g-C_3N_4. The reactive species generated during the photocatalytic process should be mainly responsible for the excellent bactericidal effect of composite photocatalysts.

3.4. The influences of pH and humic acid

A series of experiments were conducted to investigate the influence of pH and humic acid to the disinfection efficiency. The influence of pH was evaluated because the solution pH was usually considered as a vital factor affecting the absorption and photocatalytic process. In addition, wastewater fouled with bacteria could be variant in pH. As demonstrated in Fig. S7, the disinfection efficiencies of Ag(3)/g-C_3N_4 (100 μg/mL) had almost no change at different pH (6.2, 7.2, 8.2) after 1.5 h of irradiation. The solution pH is thought to be an important factor affecting the photocatalytic efficiency, since the adsorption effect of pollutants on the photocatalyst is related to the solution pH. A better adsorption effect is expected to result in better degradation effect, because of the short lifetime and easy recombination of free charge carriers. However, it had been reported that direct contact between photocatalyst and bacterial cells was not necessary for photocatalytic inactivation in some situations [9]. Herein, it was the strong oxidization power of reactive species that should be responsible for this pH independent. The high adaptability of Ag(3)/g-C_3N_4 to different pH justified its potential application in disinfecting actual wastewater with microbial contamination.

Humic acid (HA) is the main component of natural organic matter and widely exists in water. It is a kind of chemically hetero-

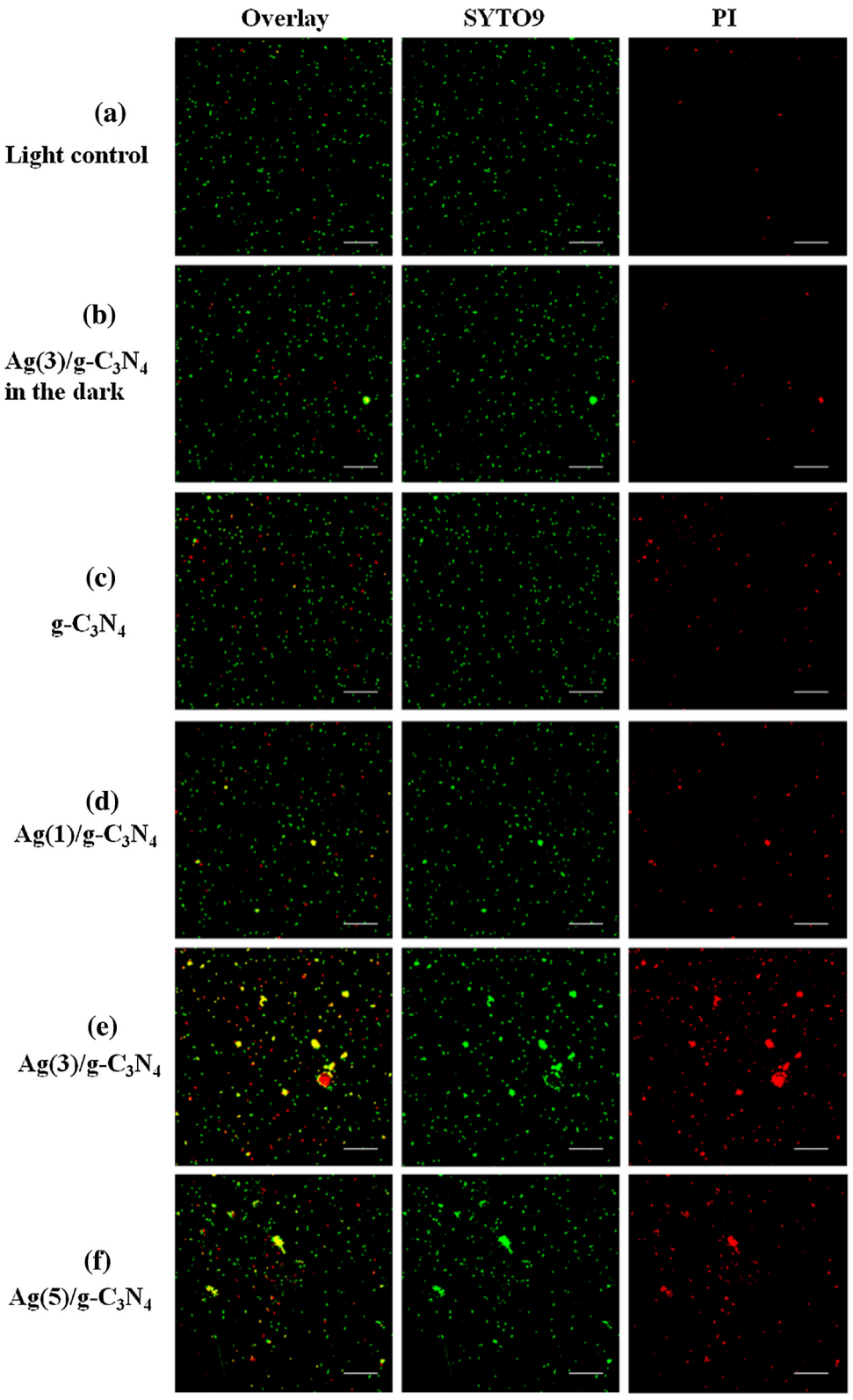

Fig. 4. Confocal fluorescent images of live and dead *E. coli* (10^9 cfu/mL) of light control (a), treated with 100 μg/mL of Ag(3)/g-C_3N_4 in the dark (b), g-C_3N_4 (c), Ag(1)/g-C_3N_4 (d), Ag(3)/g-C_3N_4 (e), and Ag(5)/g-C_3N_4 (f) under visible light irradiation for 90 min. Blue fluorescence shows both live and dead *E. coli*, and red fluorescence shows only dead *E. coli*. The scale bar is 50 μm. (For interpretation of the references to color in this figure legend, the reader is referred to the web version of this article.)

geneous compound containing abundant functional groups such as amine, hydroxyl, and carboxyl. It had been reported that HA could react with chlorine during water treatment, producing carcinogens such as trihalomethanes [41]. In this work, the impacts of HA with different concentrations on the disinfection efficiency was investigated. Based on our result in Fig. S8, it could be found that HA considerably affected the disinfection efficiency, and the effects of HA exhibited an obvious concentration dependence. Particularly, in

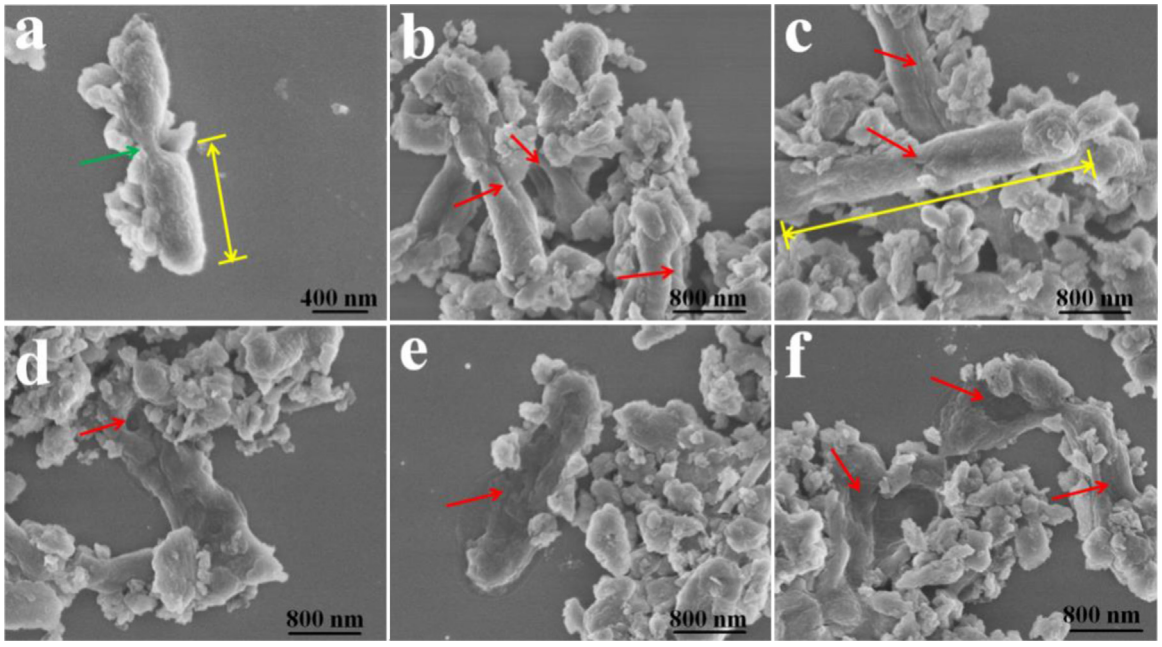

Fig. 5. SEM images of *E. coli* treated with Ag(3)/g-C_3N_4 (100 μg/mL) under visible light: (a) 0 min, (b) 30 min, (c) 45 min, (d) 60 min, (e) 75 min, (f) 90 min. The green arrow indicates the possibly cellular division. The yellow double arrows and lines are intended to measure the length of *E. coli*. The red arrows indicate the deformation, pore-forming and fracture of *E. coli*. (For interpretation of the references to color in this figure legend, the reader is referred to the web version of this article.)

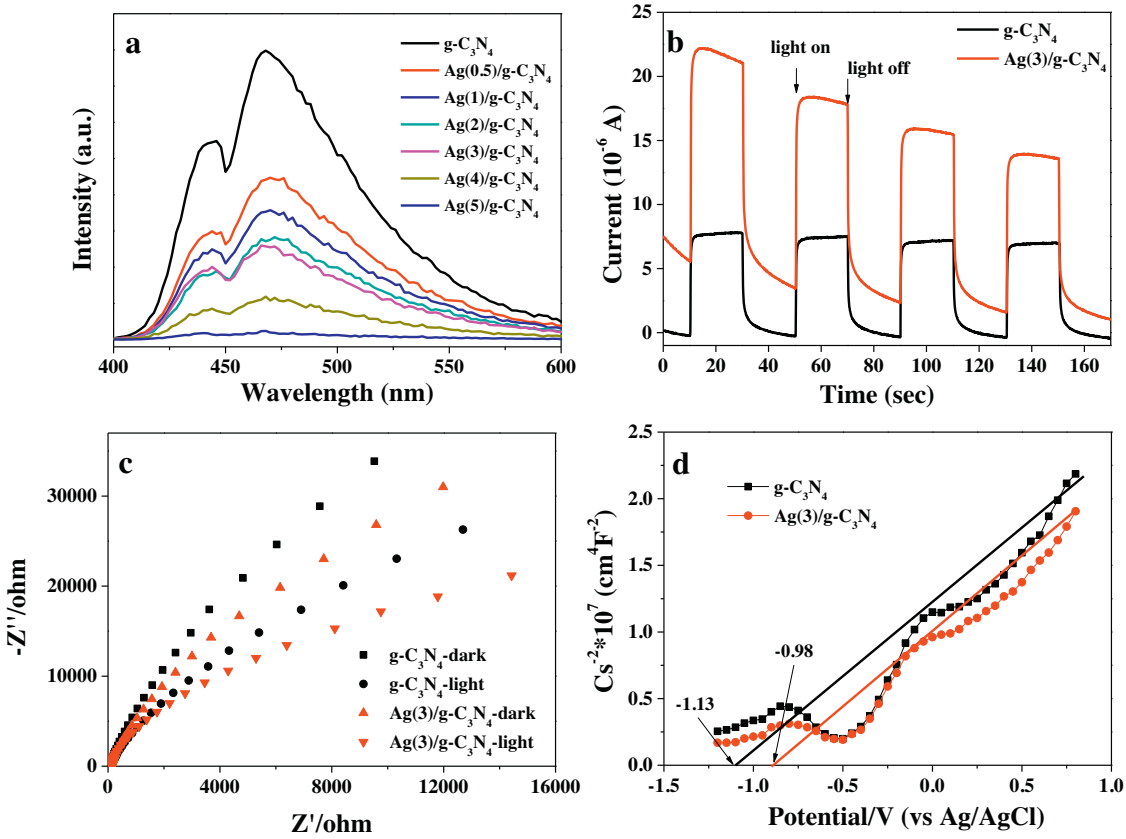

Fig. 6. PL spectra of g-C_3N_4 and Ag/g-C_3N_4 (a), Photocurrent responses (b), EIS spectra (c), and Mott–Schottky plots (d) of g-C_3N_4 and Ag(3)/g-C_3N_4.

presence of 0.5 mg/L HA, the disinfection efficiency of Ag(3)/g-C_3N_4 almost remained unchanged compared with that of in absence. At HA concentration of 1 mg/L, although HA decreased the disinfection rates from 0 to 75 min compared with that of 0.5 mg/L, the disinfection rate increased from 75 min and the final disinfection efficiency was almost same as that of 0.5 mg/L. With the further increase of HA concentrations to 2 and 5 mg/L, the final disinfection efficiency was significantly decreased compared with these of 0.5 and 1 mg/L, respectively. Possible explanations for this phenomenon may be that, at higher HA concentration, the humic acid

can be the competitor with bacteria for reactive species. The cell membrane and cell wall of *E. coli* are mainly composed of peptidoglycan layer, lipopolysaccharide layer, and phospholipid bilayer, which exhibit carboxyl, amidogen, and hydroxyl groups on their surface [42]. In addition, most nucleic acid, proteins, and other biomacromolecules had aromaticity. Aromaticity is also an important character of humic acid substances [43]. So it is reasonable to speculate that the *E. coli* and humic acid may be combined by hydrogen bond and π–π stacking interactions. In addition, Moura et al. conducted a comparative study of the adsorption of humic acid and fulvic acid onto *Bacillus subtilis* and revealed that humic acid was easier to be absorbed by the bacteria [44]. Cantwell et al. found that there was an affinity between humic acid and *E. coli* surfaces when they studies the interactions between humic acid matter and bacteria under UV light for disinfection [45]. If the humic acid substances were absorbed on the surface of *E. coli*, the disinfection efficiency was quite possible to be influenced since the cell membrane and cell wall were the foremost targets to be attacked by reactive oxygen species [42]. Moreover, it had been reported that humic acids could offer protective effect to *E. coli* against adverse illumination by absorbing light over wavelengths from 270 to 500 nm [46].

3.5. Cell integrity destruction induced by Ag(3)/g-C_3N_4

It is necessary to understand the disinfection mechanism comprehensively for maximizing the photocatalytic disinfection efficiency of Ag(3)/g-C_3N_4. As shown in Fig. 5, the morphology of *E. coli* at different stages of photocatalytic process was investigated by SEM technology. After mixing with Ag(3)/g-C_3N_4 directly, the *E. coli* cells were absorbed by the composite and exhibited an intact and smooth membrane as well as normal rod-shaped morphology with lengths about 1 μm (Fig. 5a). It seems that the two *E. coli* cells have just finished cellular division as indicated by the green arrow in Fig. 5a. After only 30 min-exposure, the adsorbed bacteria had become deformed and the cell wall wrinkled with small bulges and pits (Fig. 5b) which indicated that the active species including h^+ and $^{\bullet}O_2^-$ had been rapidly produced, contacted with the surface of *E. coli* and began to oxidize the out membrane of the cells. As shown in Fig. 5c, after 45 min of irradiation, small holes appeared on their surface, which were possibly attributed to the attacks of different reactive species. Particularly, the bacteria were about 5 times longer compared with these before irradiation as indicated by the yellow double arrow. Cell elongation is a typical SOS response of cell under detrimental situations such as exposure to biocides and UV irradiation [47]. When suffering from the stress of oxidation, *E. coli* would activate the RecA protein to inhibit the DNA replications, a very sensitive and crucial metabolic process, and further the cell division was inhibited. However, the cell biomass kept increasing during this process, so the cell became elongated [48]. As shown in Fig. 5d, after 1 h of irradiation, the strains also presented extensive cracked cell walls and membranes. Remarkably, some of the cells were even drilled by Ag(3)/g-C_3N_4 forming big cavities on cell surfaces which could cause the leakage of internal cell contents as indicated by the red arrow. As the irradiation extended to 75 min (Fig. 5e), the cell shape was seriously distorted and the cell membrane was greatly fractured, which promoted the entrance of reactive species and further the degradation of intracellular components. The *E. coli* cell was totally distorted after 90 min of irradiation as exhibited in Fig. 5f. The cell residue was tightly embedded in the Ag(3)/g-C_3N_4. It is difficult to distinguish the original morphology of *E. coli* since they have thoroughly been torn by the reactive species.

3.6. The mechanism of enhanced photocatalytic inactivation effect of Ag(3)/g-C_3N_4

To understand the optical properties of as-prepared samples, the UV–visible diffuse reflectance (UV–vis DRS) spectra of as-prepared samples were conducted (Fig. S9). It was found that pure g-C_3N_4 absorbed UV to visible light with an absorption edge at 450 nm, suggesting its visible-light-driven photocatalytic activity. The g-C_3N_4 here had the band gap of 2.7 eV, which was corresponding to the previous reported results [16,39]. After Ag nanoparticles were loaded, the absorptions in visible light region were significantly increased and the absorption edges shift toward high wavelength, consistent with the color changes from yellow to gray with the increase of Ag amounts. This phenomenon was possibly attributed to the SPR effect of Ag nanoparticles and a charge-transfer transition between Ag species and g-C_3N_4 nanosheets [31]. As we all known, noble metal nanoparticles including Au, Ag, Pt display a SPR effect that significantly enhances the light absorption [12]. Additionally, based on the results of bacterial inactivation, photocatalysts with high absorption in the visible-light region had indeed better disinfection performances than these low. Moreover, two new absorption peaks appeared in visible-light region (500–750 nm) in all the samples, and their intensities were enhanced along with the increase of Ag amounts. It had been reported that the absorption edge of carbon nitride was influenced by the preparation method including the choice of precursors and condensation temperature [37]. These two peaks in the visible-light region were beneficial for the photocatalytic activities.

Photoluminescence spectra (PL spectra) were conducted to investigate the migration, transfer, and recombination processes of photogenerated electron–hole pairs in the photocatalyst, because PL emission originated from the recombination of free charge carriers. The PL spectra of as-prepared samples at the excitation wavelength of 368 nm are exhibited in Fig. 6a. It can be observed that the emission peaks of all samples center at about 475 nm. The emission peak intensity of the Ag/g-C_3N_4 composites gradually decreased along with the increase of Ag amounts, and the peak was almost be quenched for Ag(5)/g-C_3N_4 with the highest Ag content. A weaker intensity of emission peak indicates a lower recombination possibility of photogenerated charge carriers. Therefore, incorporation of Ag nanoparticles on the surface of g-C_3N_4 nanosheets could reduce the charge recombination rate, since the Ag species acted as electron sinks, efficiently trapped photogenerated electrons from the conduct band of g-C_3N_4, and hampered the recombination of free charge carriers [32].

g-C_3N_4 and Ag(3)/g-C_3N_4 were selected to further study the internal mechanism of enhanced disinfection efficiency after Ag modification by photocurrent responses, electrochemical impedance spectroscopy (EIS) tests, and Mott–Schottky (MS) plots. The photocurrents generated from the both photocatalysts were measured under visible light with several on-off cycles. As shown in Fig. 6b, the photocurrent response of the Ag(3)/g-C_3N_4 was significantly increased under visible light irradiation, which is about 2.0 times as high as that of g-C_3N_4. The photocurrent was formed mainly by separation and diffusion of photogenerated electrons and holes from the inner structure of photocatalyst to the free charge acceptors on its surface and in the electrolyte [11]. Therefore, the enhanced photocurrent of Ag(3)/g-C_3N_4 was ascribed to the efficient electron transfer from the conduction band of g-C_3N_4 to Ag nanoparticles [12]. The increased photocurrent from Ag(3)/g-C_3N_4 indicated less recombination of the photogenerated electron–hole pairs and longer lifetime of the free charge carriers than that of g-C_3N_4, which could account for the better disinfection efficiency of Ag(3)/g-C_3N_4.

Since EIS can be used to study the migration and interface reaction ability of the charges in photocatalytic materials, the Nyquist plots of g-C_3N_4 and Ag(3)/g-C_3N_4 were performed to investigate the effect of Ag doping. Generally, a smaller arc size reflects smaller charge transfer resistance on the electrode surface [11]. As shown in Fig. 6c, the arc radius on the EIS plots of Ag(3)/g-C_3N_4 was smaller than that of g-C_3N_4 under visible light, suggesting that the separa-

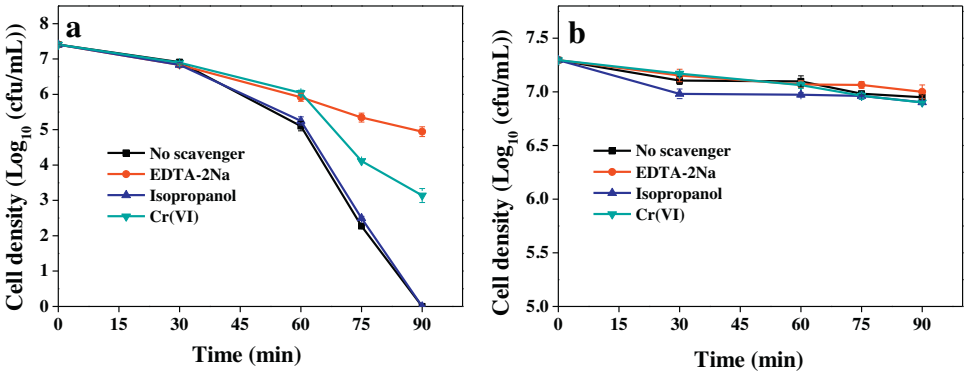

Fig. 7. Photocatalytic inactivation efficiency against *E. coli* (10^7 cfu/mL) in the presence of Ag(3)/g-C_3N_4 (a) and g-C_3N_4 (100 μg/mL) (b) with different scavengers (0.02 mmol/L Cr(VI), 0.5 mmol/L isopropanol, 0.1 mmol/L EDTA-2Na) under visible light.

tion and transfer efficiency of photoinduced electron and hole pairs was greatly increased through an interfacial interaction between g-C_3N_4 and Ag nanoparticles. The arc radius on the EIS plots of Ag(3)/g-C_3N_4 was also smaller than that of g-C_3N_4 in the dark, implying that Ag doping made charge transfer easier despite lack of light.

To further investigate the electronic properties of g-C_3N_4 and Ag(3)/g-C_3N_4, Mott–Schottky plots were carried out to study relation between capacitance of the space charge region and the applied potential. Obviously, sigmoidal plots are observed in Fig. 6d, indicating that both the photocatalysts were n-type semiconductors, which was consistent with the result from Bai et al. [11]. According to the intersection of linear potential curve at $Cs^{-2} = 0$, the flat band potential of g-C_3N_4 and Ag(3)/g-C_3N_4 is −1.13 V and −0.98 V, respectively. Therefore, the flat potential exhibited a positive shift after Ag modification. The valence band position can be estimated by the flat band potential and bandgap energy, since the conduction band position is close to the flat band potential [19]. On the basis of UV–vis DRS results, the band gap of Ag(3)/g-C_3N_4 was almost same as that of g-C_3N_4. Thus, the valence band edge of Ag(3)/g-C_3N_4 is upshifted by 0.15 V compared with that of g-C_3N_4. In general, photocatalyst with lower valence band edge produces holes with stronger oxidation ability, further resulting in better disinfection efficiency. Therefore, the enhanced disinfection efficiency of Ag(3)/g-C_3N_4 compared with g-C_3N_4 could be explained in terms of reduced recombination of free charges, rapid separation and transportation of photogenerated electrons–holes, and high oxidation power of VB holes after Ag doping.

3.7. Photocatalytic inactivation mechanism

During photocatalytic disinfection process, the h^+, •OH, H_2O_2 and $•O_2^-$ are usually considered to be the reactive oxidative species responsible for the bactericidal activity [5]. Since understanding which species played the most prominent role in the photocatalytic inactivation process was significant for improving the disinfection effect, trapping experiments of radicals and ESR technique were used to measure the reactive oxygen species generated during the photocatalytic process. The scavengers used in this study are Cr(VI) for electron [5], isopropanol for •OH [8], ethylenediamine tetraacetic acid disodium salt (EDTA-2Na) for hole [11]. Before conducting scavenger experiments, the applied concentration of different scavengers were determined to eliminate their influence on *E. coli*. The pH of the mixture without scavengers was about 7.2, and the pH value changed from 6.71 to 7.23 after the addition of scavengers. According to the early report, this change had no obvious influences on the photocatalytic disinfection [8]. As shown in Fig. 7a, compared with that of no scavenger, the disinfection efficiency of Ag(3)/g-C_3N_4 has changed little after the addition of isopropanol to remove •OH, indicating that •OH was not a crucial reactive species in this photocatalytic process. With the addition of Cr(VI) to combine e^-, the disinfection percentage exhibited obviously decrease, suggesting the important role of e^-. The e^- could transformed into other reactive species such as $•O_2^-$ and H_2O_2, which could oxidize the out membrane of bacteria. Noticeably, in the presence of EDTA-2Na, the bactericidal efficiency of Ag(3)/g-C_3N_4 decreased significantly after 1.5 h of irradiation, suggesting that the h^+ generated at the oxidation site of Ag(3)/g-C_3N_4 was the most important reactive species during the photocatalytic disinfection process. Therefore, the major reactive species for the simulated solar photocatalytic inactivation by Ag(3)/g-C_3N_4 could be h^+ and e^-. However, for g-C_3N_4 (Fig. 7b), all the three scavengers display very little effects on the disinfection efficiency. It was possibly attributed to its poor visible light response, which resulted in a smaller quantity of reactive oxidative species and further less disinfection efficiency change after the addition of scavengers.

To further confirm the exact roles of $•O_2^-$ and •OH during photocatalytic disinfection process, ESR spectra of pure g-C_3N_4 and Ag(3)/g-C_3N_4 were performed using DMPO as radical trapper under visible light irradiation. Since $•O_2^-$ in water is very unstable and easy to disproportionate instead of reacting with DMPO, the generation of $•O_2^-$ is measured in methanol. As shown in Fig. 8, in the dark, no signals could be detected for both photocatalysts. However, under the visible light irradiation, the six characteristic peaks of the DMPO-$•O_2^-$ adducts were observed for pure g-C_3N_4 (Fig. 8a) and Ag(3)/g-C_3N_4 (Fig. 8b). The appearance of $•O_2^-$ confirmed the important role of e^- during disinfection process, because which could reduce the adsorbed O_2 into $•O_2^-$. It was found that the intensity of radical signal for Ag(3)/g-C_3N_4 was stronger than that of g-C_3N_4, suggesting that the amounts of $•O_2^-$ generated in Ag(3)/g-C_3N_4 system was more than that of g-C_3N_4. That is to say, more free electron were produced in Ag(3)/g-C_3N_4 system compared with the g-C_3N_4. The photo-electrochemical tests above have proven that Ag(3)/g-C_3N_4 is superior to g-C_3N_4 in the generation, separation and transportation of photoinduced charge pairs. Herein, the ESR result further provided a solid interpretation for the important role of Ag species on the surface of g-C_3N_4, forming heterogenous interface and acting as electron sinkers, for enhanced photocatalytic disinfection efficiency. However, for both g-C_3N_4 and Ag(3)/g-C_3N_4, four characteristic peaks of DMPO-•OH were not observed in irradiated or non-irradiated photocatalysts aqueous dispersions (data were not shown). According to the calculation by UV–vis DRS and MS plots, as shown in Fig. 9, the oxidation power of photogenerated VB-holes of Ag(3)/g-C_3N_4 is +1.72 V versus NHE, which could not oxidize the OH^- to produce •OH ($E^\theta(OH^-/•OH) = 2.40$ V versus

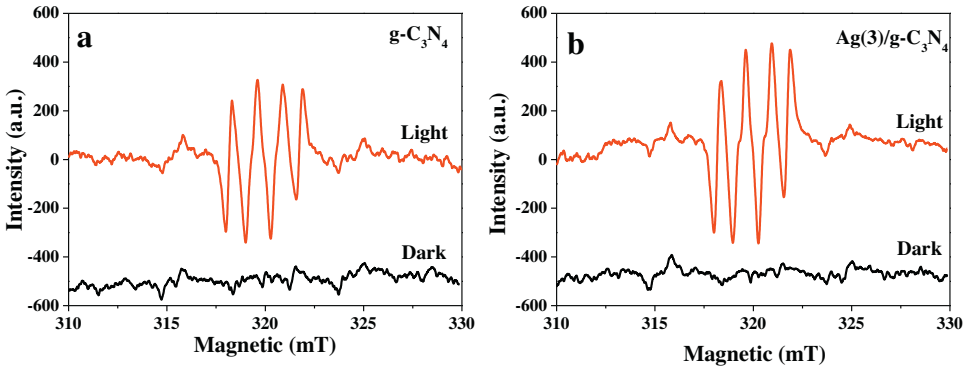

Fig. 8. ESR spectra of g-C_3N_4 (a) and Ag(3)/g-C_3N_4 (b) photocatalysts in methanol solvent with DMPO as radical trapper.

NHE). On the other hand, this absence of •OH signal is verified the result of above scavengers experiment.

According to the above reactive species research, the possible disinfection mechanism of Ag(3)/g-C_3N_4 is proposed in Fig. 10. First, water, O_2, and *E. coli* were adsorbed on the surface of Ag(3)/g-C_3N_4 plane. Second, when the visible light irradiation hit the surface of Ag(3)/g-C_3N_4 and the light energy exceeded its band gap energy (Eg), the electrons on valence band (VB) would transfer into the conduction band (CB) leaving hole (h^+) with high oxidation power on valence band. In addition, e^- transformed into conduction band could transfer to Ag nanoparticles which could trap e^- and prevent the recombination of e^- and h^+. The e^- could react with O_2 absorbed on the surface of the Ag(3)/g-C_3N_4 to form $•O_2^-$ and H_2O_2. The reactive species including h^+ and $•O_2^-$ could attack the cell wall, oxidize and tear the semipermeable membrane, causing leakages of cell inclusions, and finally the death of *E. coli* cell.

3.8. Reusability of Ag(3)/g-C_3N_4

The recovery and reusability are significant for the practical application of photocatalysts in water remediation. The reusability of Ag(3)/g-C_3N_4 was investigated by recycling the materials in three cycles. After each application, the photocatalysts were washed with sterile water three times. In Fig. S10a, all the *E. coli* cells were inactivated under 90 min of visible light exposure using Ag(3)/g-C_3N_4 as a biocide. However, the bactericidal efficiency was dramatically decreased in the second and third cycles. Concretely, only 1.55 and 0.80 log of *E. coli* cells were inactivated in the second and third cycle, respectively. According to the SEM image of *E. coli* after photocatalytically inactivated (Fig. 5f), there were amounts of cell debris that were not be degraded, which were firmly embedded on the surface of Ag(3)/g-C_3N_4. The cell debris possibly occupied the adsorption sites on the surface of Ag(3)/g-C_3N_4, which was unfavorable to adsorb bacteria in the next cycle. In addition, the reactive species including h^+, H_2O_2 and $•O_2^-$ produced by Ag(3)/g-C_3N_4 could firstly oxidize the cell debris embedded onto it, and then the bacteria in the salt solution. Therefore, if these cell debris were not removed from Ag(3)/g-C_3N_4, it would have an adverse influence on the multi-cycle application of the photocatalysts.

Here, a post-treating method was used to try to increase the reusability of Ag(3)/g-C_3N_4. After each disinfection application, the photocatalysts were recovered by centrifugation. Then the materials were added into 10 mL 75% of ethanol aqueous solution, dispersed by ultrasonication for 5 min, and stirred for 12 h to decompose the cell debris. The materials were collected by centrifugation under 7000 rpm for 3 min and washed using sterile water several times to remove the residue ethanol. As shown in Fig. S10b, 3.59 and 2.49 log of *E. coli* cells were inactivated with Ag(3)/g-C_3N_4 applied in the second and third cycle, respectively. This illustrated that the bactericidal effect were partly recovered. The Ag(3)/g-C_3N_4 after the three cycles was covered with lots of cell debris (Fig. S11a). However, the quantity of cell debris was significantly decreased after it was dispersed by ultrasonication and soaked in 75% of ethanol aqueous solution (Fig. S11b). Although the bactericidal effect was increased by using the method here, large amounts of endeavors including investigating novel post-treating methods and developing new-structured nanomaterials should be made for reusing the photocatalysts efficiently in the practical application.

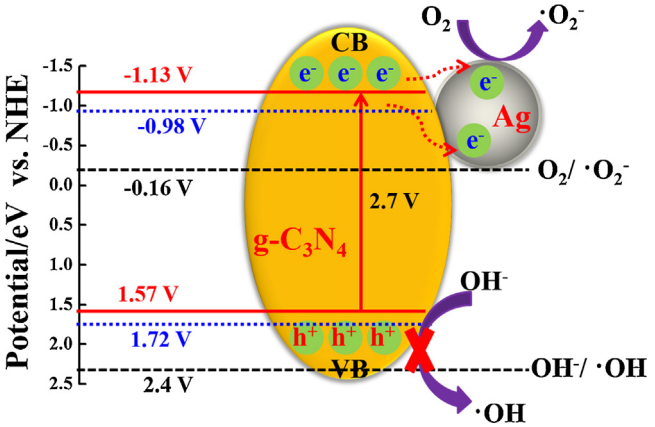

Fig. 9. Generation, separation and transportation of h^+ and e^- at the interface of Ag/g-C_3N_4 under visible light irradiation.

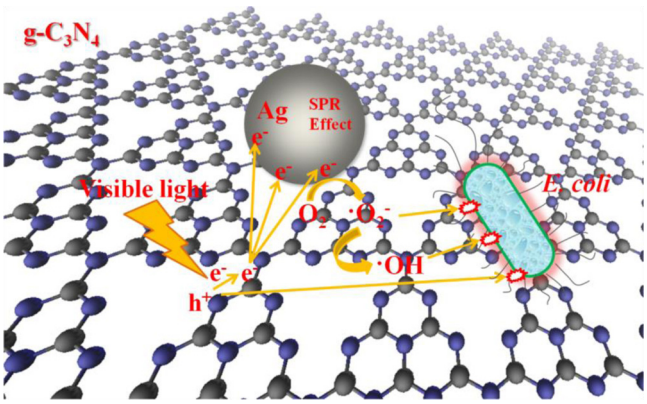

Fig. 10. The mechanism of *E. coli* inactivation in the presence of Ag/g-C_3N_4 under visible light.

4. Conclusions

Novel visible-light-driven Ag/g-C_3N_4 plasmonic photocatalysts were synthesized by the method combining thermal polymerization of melamine precursor with photo-reduction approach. It was found that Ag nanoparticles were well dispersed on the surface of g-C_3N_4. The doping of Ag species did not change the crystal structure and morphology of g-C_3N_4. The composite photocatalysts exhibited significantly enhanced photocatalytic disinfection efficiency than pure g-C_3N_4 powders. The best disinfection efficiency was observed with Ag(3)/g-C_3N_4 sample. The Ag(3)/g-C_3N_4 still maintained excellent disinfection efficiency at different pH (6.2, 7.2, and 8.2) and in presence of low concentration of humic acid (<1 mg/L). The Ag(3)/g-C_3N_4 treatment could cause the destruction of cell wall and membrane and further the leakages of cellular inclusions. The mechanism of enhanced disinfection activity was studied by UV–vis DRS, PL spectra, and photo-electrochemical methods including photogenerated current densities, EIS spectra and MS plots. The enhanced photocatalytic bactericidal effect was attributed to the hybrid effect from Ag and g-C_3N_4, which resulted in enhanced adsorption of visible light, reduced recombination of free charges, rapid separation and transportation of photogenerated electrons–holes, and long lifetime of charge carriers. The disinfection mechanism was studied by employing chemical scavengers and ESR technology, suggesting the important role of h^+, e^-, and $^{\bullet}O_2^-$. Taking into consideration the bulk availability and excellent disinfection activity of Ag/g-C_3N_4, this paper provided a new approach in designing visible-light-driven photocatalyst for water disinfection.

Acknowledgments

The authors gratefully acknowledge the financial support provided by the National Natural Science Foundation of China as general projects (21377061 and 31170473), and a joint Guangdong project (U1133006), and the Key Technologies R&D Program of Tianjin (13ZCZDSF00300).

Appendix A. Supplementary data

Supplementary data associated with this article can be found, in the online version, at http://dx.doi.org/10.1016/j.apcatb.2015.12.051 .

References

[1] S.S. Philip, J.W. Costerton, E.P. Greenberg, Science 284 (1999) 1318–1322.
[2] S.L. Ma, S.H. Zhan, Y.N. Jia, Q.X. Zhou, ACS Appl. Mater. Interfaces 7 (2015) 10576–10586.
[3] J. Podporska-Carroll, E. Panaitescu, B. Quilty, L.L. Wang, L. Menon, S.C. Pillai, Appl. Catal. B: Environ. 176 (2015) 70–75.
[4] S.L. Cates, E.L. Cates, M. Cho, J.H. Kim, Environ. Sci. Technol. 48 (2014) 2290–2297.
[5] Y.M. Chen, A.H. Lu, Y. Li, L.S. Zhang, H.Y. Yip, H.J. Zhao, T.C. An, P.K. Wong, Environ. Sci. Technol. 45 (2011) 5689–5695.
[6] T. Matsunaga, R. Tomoda, T. Nakajima, H. Wake, FEMS Microbiol. Lett. 29 (1985) 211–214.
[7] M.A. Shannon, P.W. Bohn, M. Elimelech, J.G. Georgiadis, B.J. Marinas, A.M. Mayes, Nature 452 (2008) 301–310.
[8] W.J. Wang, T.W. Ng, W.K. Ho, J.H. Huang, S.J. Liang, T.C. An, G.Y. Li, J.C. Yu, P.K. Wong, Appl. Catal. B: Environ. 129 (2013) 482–490.
[9] L.S. Zhang, K.H. Wong, H.Y. Yip, C. Hu, J.C. Yu, C.Y. Chan, P.K. Wong, Environ. Sci. Technol. 44 (2010) 1392–1398.
[10] M.T. Guo, J.J. Huang, H.Y. Hu, W.J. Liu, J. Yang, Water Res. 46 (2012) 4031–4036.
[11] X.J. Bai, L. Wang, Y.J. Wang, W.Q. Yao, Y.F. Zhu, Appl. Catal. B: Environ. 152–153 (2014) 262–270.
[12] R.C. Pawar, Y.J. Pyo, S.H. Ahn, C.S. Lee, Appl. Catal. B: Environ. 176 (2015) 654–666.
[13] X.C. Wang, K. Maeda, A. Thomas, K. Takanabe, G. Xin, J.M. Carlsson, K. Domen, M. Antonietti, Nat. Mater. 8 (2009) 76–80.
[14] K.X. Li, Z.X. Zeng, L.S. Yan, S.L. Luo, X.B. Luo, Appl. Catal. B: Environ. 165 (2015) 428–437.
[15] H.X. Zhao, H.T. Yu, X. Quan, S. Chen, Y.B. Zhang, H.M. Zhao, H. Wang, Appl. Catal. B: Environ. 152–153 (2014) 46–50.
[16] Y.X. Yang, Y.N. Guo, F.Y. Liu, X. Yuan, Y.H. Guo, S.Q. Zhang, W. Guo, M.X. Huo, Appl. Catal. B: Environ. 142–143 (2013) 828–837.
[17] Y.M. He, Y. Wang, L.H. Zhang, B.T. Teng, M.H. Fan, Appl. Catal. B: Environ. 168–169 (2015) 1–8.
[18] Y.Y. Bu, Z.Y. Chen, W.B. Li, Appl. Catal. B: Environ. 144 (2014) 622–630.
[19] M. Zhang, X.J. Bai, D. Liu, J. Wang, Y.F. Zhu, Appl. Catal. B: Environ. 164 (2015) 77–81.
[20] Y.L. Tian, B.B. Chang, J.L. Lu, J. Fu, F.N. Xi, X.P. Dong, ACS Appl. Mater. Interfaces 5 (2013) 7079–7085.
[21] J. Chen, S.H. Shen, P.H. Guo, M. Wang, P. Wu, X.X. Wang, L.J. Guo, Appl. Catal. B: Environ. 152–153 (2014) 335–341.
[22] S.W. Cao, X.F. Liu, Y.P. Yuan, Z.Y. Zhang, Y.S. Liao, J. Fang, S.C.J. Loo, T.C. Sum, C. Xue, Appl. Catal. B: Environ. 147 (2014) 940–946.
[23] G.S. Li, Z.C. Lian, W.C. Wang, D.Q. Zhang, H.X. Li, Nano Energy (2015), http://dx.doi.org/10.1016/j.nanoen.2015.10.011.
[24] Y.J. Zhou, L.X. Zhang, J.J. Liu, X.Q. Fan, B.Z. Wang, M. Wang, W.C. Ren, J. Wang, M.L. Li, J.L. Shi, J. Mater. Chem. A 7 (2015) 3862–3867.
[25] W.J. Wang, J.C. Yu, D.H. Xia, P.K. Wong, Y.C. Li, Environ. Sci. Technol. 47 (2013) 8724–8732.
[26] H.X. Lin, W.H. Deng, T.H. Zhou, S.B. Ning, J.L. Long, X.X. Wang, Appl. Catal. B: Environ. 176 (2015) 36–43.
[27] W.J. Ong, L.L. Tan, S.P. Chai, S.T. Yong, Dalton Trans. 44 (2015) 1249–1257.
[28] J.J. Xue, S.S. Ma, Y.M. Zhou, Z.W. Zhang, M. He, ACS Appl. Mater. Interfaces 7 (2015) 9630–9637.
[29] Y.X. Yang, W. Guo, Y.N. Guo, Y.H. Zhao, X. Yuan, Y.H. Guo, J. Hazard. Mater. 237 (2012) 331–338.
[30] S.F. Kang, Y. Fang, Y.K. Huang, L.F. Cui, Y.Z. Wang, H.F. Qin, Y.M. Zhang, X. Li, Y.A. Wang, Appl. Catal. B: Environ. 168–169 (2015) 472–482.
[31] X.J. Bai, R.L. Zong, C.X. Li, D. Liu, Y.F. Liu, Y.F. Zhu, Appl. Catal. B: Environ. 147 (2014) 82–91.
[32] L. Ge, C.C. Han, J. Liu, Y.F. Li, Appl. Catal. A: Gen. 409–410 (2011) 215–222.
[33] J.T. Li, S.K. Cushing, J. Bright, F.K. Meng, T.R. Senty, P. Zheng, A.D. Bristow, N.Q. Wu, ACS Catal. 3 (2013) 47–51.
[34] D.B. Ingram, P. Christopher, J.L. Bauer, S. Linic, ACS Catal. 1 (2011) 1441–1447.
[35] S.W. Cao, Z. Yin, J. Barber, F.Y.C. Boey, S.C.J. Loo, C. Xue, ACS Appl. Mater. Interfaces 4 (2011) 418–423.
[36] G. Xiao, X. Zhang, W.Y. Zhang, S. Zhang, H.J. Su, T.W. Tian, Appl. Catal. B: Environ. 170–171 (2015) 255–262.
[37] X.C. Wang, S. Blechert, M. Antonietti, ACS Catal. 2 (2012) 1596–1606.
[38] Q.Y. Lin, L. Li, S.J. Liang, M.H. Liu, J.H. Bi, L. Wu, Appl. Catal. B: Environ. 163 (2015) 135–142.
[39] L. Ge, C.C. Han, Appl. Catal. B: Environ. 117–118 (2012) 268–274.
[40] H.P. Li, J.Y. Liu, W.G. Hou, N. Du, R.J. Zhang, X.T. Tao, Appl. Catal. B: Environ. 160–161 (2014) 89–97.
[41] J. Li, S.W. Zhang, C.L. Chen, G.X. Zhao, X. Yang, J.X. Li, X.K. Wang, ACS Appl. Mater. Interfaces 4 (2012) 4991–5000.
[42] O.K. Dalrymple, E. Stefanakos, M.A. Trotz, D.Y. Goswami, Appl. Catal. B: Environ. 98 (2010) 27–38.
[43] J.L. Weishaar, G.R. Aiken, B.A. Bergamaschi, M.S. Fram, R. Fujii, K. Mopper, Environ. Sci. Technol. 37 (2003) 4702–4708.
[44] M.N. Moura, M.J. Martin, F.J. Burguillo, J. Hazard. Mater. 149 (2007) 42–48.
[45] R.E. Cantwell, R. Hofmann, M.R. Templeton, J. Appl. Microbiol. 105 (2008) 25–35.
[46] A. Muela, J.M. Garcia-Bringas, I. Arana, I. Barcina, Microb. Ecol. 40 (2000) 336–344.
[47] G. Applerot, A. Lipovsky, R. Dror, N. Perkas, Y. Nitzan, R. Lubart, A. Gedanken, Adv. Funct. Mater. 19 (2009) 842–852.
[48] T. Kawarai, M. Wachi, H. Ogino, S. Furukawa, K. Suzuki, H. Ogihara, M. Yamasaki, Appl. Microbiol. Biotechnol. 64 (2004) 255–262.